Journal of Electroceramics, 7, 35–46, 2001
© 2001 Kluwer Academic Publishers. Manufactured in The Netherlands.

Tin Oxide Thin Films Grown on the ($\bar{1}012$) Sapphire Substrate

X.Q. PAN & L. FU

Department of Materials Science and Engineering, The University of Michigan, Ann Arbor, MI 48109, USA

Submitted September 15, 2000; Revised September 15, 2000; Accepted March 1, 2001

Abstract. Tin oxide thin films were deposited on the R-cut sapphire substrate by the electron-beam evaporation of a ceramic SnO_2 source. X-ray diffraction and transmission electron microscopy studies revealed that the films deposited at lower temperatures were amorphous while those grown at temperatures above 350°C consisted of the α-SnO phase with the PbO type structure. Epitaxial α-SnO films on the R-cut sapphire substrate were obtained when deposited at 600°C. Atomic force microscopy studies showed that films deposited at low temperature have a smooth surface, while epitaxial SnO films deposited at high temperatures (above 600°C) have a relatively rough surface. The atomic mobilities in the films at the various deposition temperatures and the lattice mismatch between the films and the substrates ultimately determine the microstructure and surface mophology. X-ray photoelectron spectroscopy analysis shows that the Sn/O ratios are 52.7/47.6 for the amorphous film deposited at the ambient temperature ($\sim$30°C), 48.8/51.2 for the films deposited at 350°C, and 49.2/50.8 for the epitaxial film deposited at 600°C. Electrical properties were determined by four point probe measurements.

Keywords: Tin oxide, Sno, thin film, microstructure, TEM, electron beam deposition

1. Introduction

Stannic oxide (SnO_2) with the rutile type crystal structure is an n-type wide band gap semiconductor. Owing to its high chemical and mechanical stability, it is extensively used in many applications such as solar cells, catalytic support materials, transparent electrodes, and gas-sensors [1, 2]. SnO_2 is widely used as a base material in gas alarms on domestic, commercial, and industrial premises due to its high sensitivity to small concentrations of gases (at ppm levels). In particular, SnO_2 thin films have drawn much interest because of their potential application in microsensor devices [3]. Considerable attention has recently focused on the development of solid state gas sensors based on thin films with a crystallite size smaller than the Debye length of the material. Such sensors show an increased gas sensitivity and short response time [4, 5]. Thus, due to its simple rutile structure, SnO_2 is an ideal model for a systematic investigation of the effect of the microstructure on the electrical properties of oxides.

Various thin film deposition techniques have been used to fabricate tin oxide films, including sputtering [6–8], electron-beam evaporation [9, 10], chemical vapor deposition [11, 12], and spray pyrolysis [13, 14]. Sintered SnO_2 ceramics are commonly used as starting source material for the synthesis of tin oxide films by physical vapor deposition. However, the SnO_2 molecules decompose at high temperature in the gaseous state [15]. As a result, either amorphous phase or metastable crystalline SnO_x films are formed under high vacuum conditions in the PVD chamber, depending on the substrate temperature. A subsequent post-deposition annealing step is required in order to obtain a SnO_2 film with the rutile structure. In contrast to the extensive studies on SnO_2 [1, 2, 16–20], thin films of the SnO phase are rarely investigated. Since SnO is the starting material for the formation of the rutile type SnO_2 during the anneal (oxidation) in oxygen atmosphere, its microstructure and orientation relationship with respect to the substrate materials will strongly influence the microstructure and surface morphology of the resulting SnO_2 films. This in turn will determine the properties, performance and reliability of the SnO_2 films [21]. Therefore, a systematic investigation of these precursor SnO films is necessary for

a comprehensive understanding of the microstructure-property relationships of SnO_2 thin films. In this paper, we present the results of our studies on SnO_x thin films fabricated by an electron-beam evaporation deposition of a ceramic SnO_2 source.

2. Experimental

2.1. *Preparation of Source Materials*

Chemical coprecipitation was used to prepare the high purity tin oxide powder that later would be used to produce the target material for the thin film deposition. An aqueous solution of $SnCl_4$ was made by dissolving $SnCl_4{\cdot}5H_2O$ (Alfa Aesar, MA) in distilled water. A small amount of hydrochloric acid was added into the solution to avoid the formation of $SnO(OH)_2$. The solution was then stirred on a magnetic plate. In the meantime, aqueous NH_3 solution was gradually added to neutralize the solution and obtain tin hydroxide precipitates. The reaction is described by:

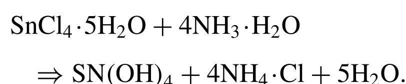

$$SnCl_4{\cdot}5H_2O + 4NH_3{\cdot}H_2O \Rightarrow SN(OH)_4 + 4NH_4{\cdot}Cl + 5H_2O.$$

The precipitates were thoroughly washed with distilled water and filtered through a 0.2 μm membrane filter several times. The final condensed precipitates were dried at 80°C in a low-temperature oven for 20 hours. The resulting granules were then broken down by grinding to form a white powder of tin hydroxide. Tin oxide powders with the rutile structure were obtained by calcinating the tin hydroxide powders at elevated temperature (700°C). Discs of 1.25 cm in diameter and 1.25 cm thickness for e-beam deposition were made by sintering at 1200°C for one hour in air.

2.2. *Film Deposition*

Figure 1 is a schematic drawing of the e-beam evaporation deposition system. The high purity SnO_2 ceramic source was loaded into a crucible, as shown in Fig. 1. The substrate materials used in this study were single-crystal Al_2O_3 (sapphire) with a $(\bar{1}012)$ surface orientation (R-cut). After loading the substrate into the deposition chamber, the system was pumped down to approximately 5.0×10^{-8} Torr. The substrates were mounted on a tantalum wire heating hot stage, which can be heated to as high as 1200°C. During deposition, the background pressure in the chamber was about 10^{-6} Torr. Films were deposited at different temperatures between ambient temperature (∼25°C) to 600°C with a nominal film thickness around 1000 Å. A quartz crystal oscillator installed within the deposition chamber was used to measure the deposition rate. The film thickness measurement was determined by cross-section TEM. The deposition rate for this study was 0.4 Å/sec.

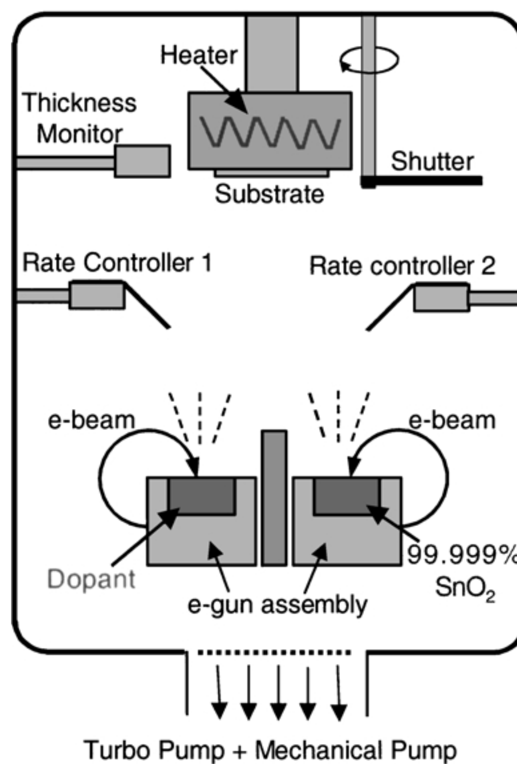

Fig. 1. Schematic of electron beam deposition chamber for the tin oxide thin film deposition.

2.3. *Characterization of Thin Films*

Thin film microstructures were characterized by X-ray diffraction, atomic force microscopy (AFM), and transmission electron microscopy (TEM). For the X-ray diffraction studies, both θ–2θ scans and pole figures were measured on a rotating anode four-circle diffractometer (Rigaku, Japan) using Cu-Kα radiation. AFM studies were performed on a Nanoscope III atomic force microscope (Digital Instruments, Inc., CA) operated in tapping mode and using etched silicon tips (Digital Instruments, Inc., CA).

Both plan-view and cross-section TEM specimens were prepared by a standard procedure, which includes

mechanical grinding, polishing, precision dimpling and ion-milling. The final thinning of specimens was carried out on a Gatan Precision Ion Polishing System (PIPS^{TM}, Model 691) using an accelerating voltage of 4.5 kV and an incident angle of 4–6°. All specimens were investigated in a JEOL JEM 4000EX high-resolution transmission electron microscope (HRTEM) equipped with a Gatan Imaging Filter (GIF), operated at 400 kV, with a point resolution of 0.17 nm.

Chemical composition analysis was performed on a PHI 5400 x-ray photoelectron spectroscope (Perkin-Elmer Corporation, MN). All spectra were recorded under vacuum conditions better than 10^{-9} Torr. The electrical properties of the thin films were determined using a four point probe.

3. Results

The three different thin films deposited by e-beam evaporation of a SnO_2 ceramic source studied in this work were: E-600 deposited at 600°C, E-350 at 350°C and E-RT at the ambient temperature (∼30°C), respectively. Except for the deposition temperature, all film deposition conditions were identical. Figure 2 shows x-ray diffraction patterns for all three samples. For the film E-RT [curve (a)] no reflections were observed except for the two strong peaks located at 25.6° and 52.5°

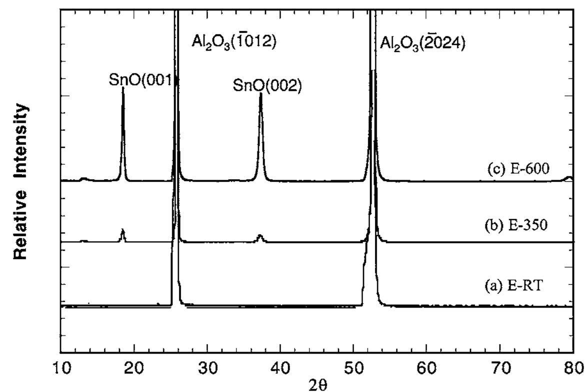

Fig. 2. θ–2θ x-ray diffraction patterns of tin oxide thin films fabricated by the electron beam evaporation of a ceramic SnO_2 source: (a) for the film deposited at room temperature (E-RT), (b) for the film deposited at 350°C (E-350), and (c) for the film deposited at 600°C (E-600). The strong peaks at 25.6° and 52.5° for 2θ correspond to the $10\bar{1}2$ and $20\bar{2}4$ reflections of the sapphire substrate (α-Al_2O_3). Note that film E-RT is amorphous while films E-350 and E-600 are crystalline with the α-SnO structure.

for 2θ. These peaks correspond to the $\bar{1}012$ and $\bar{2}024$ reflections of the sapphire substrate. Cross-section TEM investigations revealed that this film has an amorphous structure. For the E-350 film [curve (b)] two peaks located at 18.3° and 37.2° appear, in addition to the strong reflections from the substrate. These two peaks are found to be consistent with the 001 and 002 reflections of the tetragonal α-SnO phase with the PbO-type structure (space group $P4/nmm$) [22]. A similar x-ray diffraction pattern was obtained for film E-600 [curve (c)] except that the peak intensities from this film were higher than those from film E-350. These results reveal that the film deposited at ambient temperature is amorphous, while those grown above 350°C are composed of the α-SnO structure. Since only (001) and (002) reflections were observed in the crystalline α-SnO films (E-350 and E-600), which typically are not the strongest peaks in the powder diffraction pattern for α-SnO, the films must be strongly textured with an out-of-plane orientation relationship with respect to the substrate of $(001)_{SnO}//(\bar{1}012)_{sapphire}$.

The surface morphologies of these films were investigated by AFM. Figure 3 shows AFM images taken from the same SnO films as for the x-ray studies described above. Film E-RT, which is amorphous according to both x-ray diffraction and TEM studies, has a relatively smooth surface with the root mean square (rms) roughness of ∼2.2 nm [Fig. 3(a)]. The film consists of many small spherical agglomerates with a typical size of about 30 nm. Film E-350 has a very smooth surface with rms roughness equal to 1.1 nm [Fig. 3(b)]. Small grains are uniformly distributed along the film surface with a mean size of ∼30 nm. However, a much rougher surface was found in the film E-600, with rms roughness of ∼8.1 nm [Fig. 3(c)]. This high roughness (film E-600) is due to the existence of many hillocks, which are faceted and distributed randomly on the relatively smooth surface. This feature is seen in the cross-section TEM image, Fig. 4(a), taken from a cross-sectional specimen of the as-grown E-600 film. The thin film has a thickness of about 120 nm and shows a smooth surface in most of the areas except for some small areas with a well-faceted shape. Fig. 4(a) also shows that the grains in the film have a columnar structure. The average diameter of the grains, determined from the cross-section TEM images, is about 150 nm. Figure 4(b) shows a selected area electron diffraction (SAED) pattern taken from an area including both the substrate and the thin film. This pattern corresponds

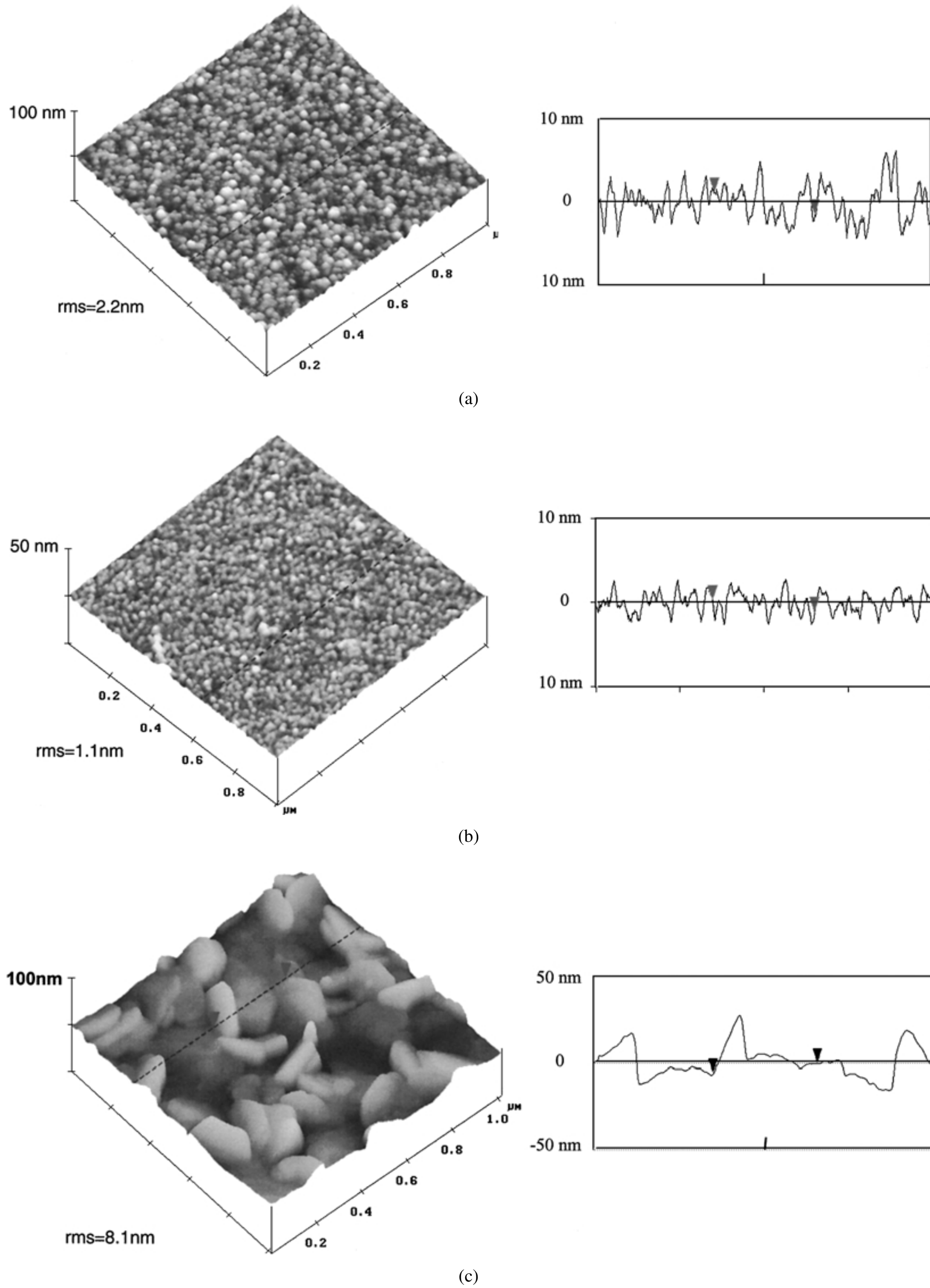

Fig. 3. Atomic force microscopic (AFM) images and surface profiles of tin oxide thin films deposited by electron beam deposition: (a) film E-RT, (b) film E-350, and (c) film E-600.

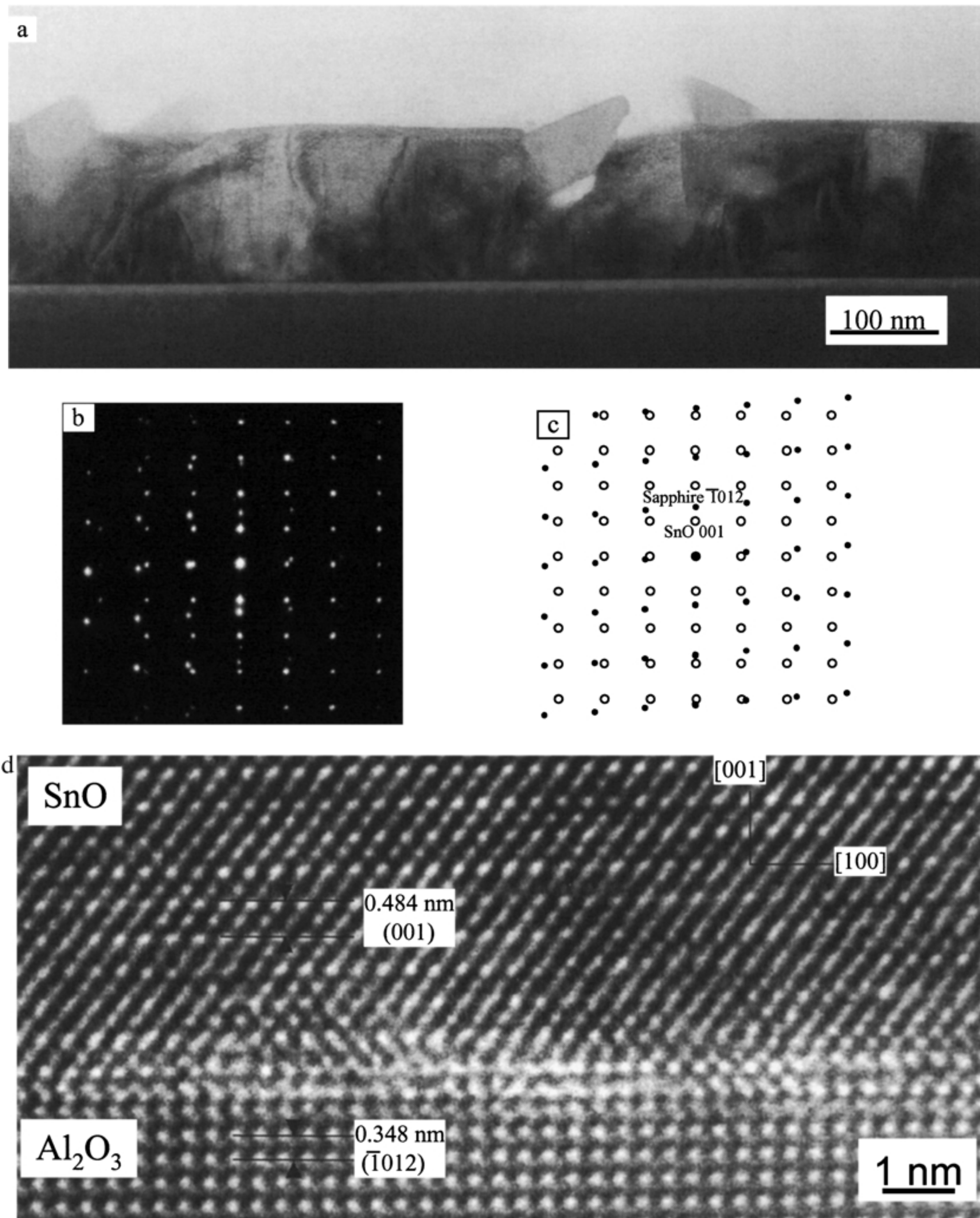

Fig. 4. (a) Cross-section TEM image of film E-600. (b) Electron diffraction taken from an area, which includes both the sapphire substrate and the SnO film, of the same film as for (a). (c) Schematic showing the superposition of two sets of diffraction patterns shown in (b), which belong to the [2$\bar{2}$01] zone diffraction pattern of the sapphire substrate (open circles) and the [100] zone diffraction of the α-SnO structure (filled circles). (d) HRTEM micrograph taken from the same cross-section specimen as for (a), with the electron beam aligned parallel to the SnO [100] direction which is parallel to the Al_2O_3 [2$\bar{2}$01] direction.

to the superposition of two sets of diffraction patterns: one corresponds to the $[2\bar{2}01]$ zone diffraction pattern of the α-Al_2O_3 structure (the sapphire substrate), the other is the [100] zone diffraction of the α-SnO structure (the film). An schematic showing the overlapping of the two diffraction patterns is given in Fig. 4(c). It is seen that the orientation relationship between the film and the substrate is given by $(001)_{SnO}//(\bar{1}012)_{Al_2O_3}$ (the sapphire R-plane) out of the plane and $[100]_{SnO}//(2\bar{2}01)_{Al_2O_3}$ in the film plane. The same diffraction pattern, except for a small tilting (less than 3°) of the film along the SnO [001] direction with respect to the sapphire substrate, was observed in all thin areas of many TEM specimens cut from the same thin film. The film/substrate interface was also investigated by cross-section HRTEM. Figure 4(d) shows an HRTEM micrograph taken from the same cross-section specimen as for Fig. 4(a), with the electron beam aligned parallel to the $[100]_{SnO}$ and the $[2\bar{2}01]_{sapphire}$ directions. It is observed that the SnO/Al_2O_3 (sapphire) interface is atomically abrupt. The orientation relationship between the film and the substrate is given by $(001)[100]_{SnO}//(\bar{1}012)[2\bar{2}01]_{Al_2O_3}$.

Plan-view TEM studies were also conducted on the same thin film. Figure 5(a) is a TEM micrograph taken from a plan-view specimen which shows grains about 150 nm in average, consistent with those seen in the cross-section TEM image. Figure 5(b) is the electron diffraction pattern taken from the same area shown in Fig. 5(a). This diffraction pattern corresponds to the SnO [001] zone. The smearing intensity distribution of reflections indicates that the thin film consists of many grains which are rotated by small angles (<3°) with respect to each other along the [001] direction, i.e., the film normal. The corresponding electron diffraction pattern from the substrate is shown in Fig. 5(c). It is clear that the orientation of most of grains in the film with respect to the substrate is: $(001)[100]_{SnO}//(\bar{1}012)[2\bar{2}01]_{Al_2O_3}$, which is consistent with that determined by cross-section TEM studies. The small misorientation of SnO grains through tilting around the [001] direction results in the diffraction contrast in the TEM images as observed in both Fig. 4(a) and Fig. 5(a).

Similar TEM investigations were conducted on the E-350 film, which was grown at 350°C. Figure 6(a) is a bright field TEM image taken from a cross-section specimen, showing a smooth surface. Figure 6(b) is a TEM image taken from a plan-view specimen of the same thin film. The film consists of grains with an average diameter of ~30 nm. The electron diffraction pattern is displayed at the upper right corner of Fig. 6(b). The pattern includes both reflections from the SnO film (rings) and reflections from the sapphire substrate (distinct spots). The rings correspond to *h k 0* reflections of the α-SnO structure. These results indicate that the SnO film has an out-of-plane orientation relationship with respect to the substrate of $(001)_{SnO}//(\bar{1}012)_{Al_2O_3}$, while SnO grains are oriented randomly with each other in the (001) plane.

The chemical composition of all three films was studied using XPS. Figure 7 shows an XPS spectrum taken from film E-600, showing the binding energy peak positions for Sn 3d and O 1s. The Sn core levels $3d_{5/2}$ and $3d_{3/2}$ are observed at 486.2 eV and 494.6 eV respectively. The bonding energy peak for O 1s is located at 530.2 eV. The relative concentrations of the constituent elements were calculated by utilizing the peak area sensitivity factors. The [Sn]/[O] ratio was found to be 49.2/50.8 for film E-600. Similar studies were conducted for films E-350 and E-RT, and the [Sn]/[O] ratios were determined to be 48.8/51.2 for E-350 and 52.6/47.4 for E-RT, respectively. No impurity elements were detected in the XPS investigations.

The electrical properties of all three films at room temperature were studied by four-point probe measurements using the van der Pauw configuration. Hall measurements indicated that both films E-600 and E-350 show a *p*-type semiconducting behavior. Films E-600 and E-350 have resistivities of 195 $\Omega \cdot$ cm and 18 $\Omega \cdot$ cm respectively. However, the amorphous film E-RT has a very high resistivity of 1.4×10^8 $\Omega \cdot$cm, which can be considered as an insulator. Table 1 summarizes the microstructure, [Sn]/[O] ratio and resistivity (at room temperature) of three films.

4. Discussion

According to the present studies, the microstructure of thin films deposited on the R-cut sapphire substrates by the e-beam evaporation of a SnO_2 ceramic source depends on deposition temperatures. The film deposited at ambient temperature (~25°C) is amorphous, while those deposited at temperatures above 350°C are polycrystalline with the tetragonal α-SnO structure and consist of a strong out-of-plane texture: $(001)_{SnO}//(\bar{1}012)_{Al_2O_3}$. The in-plane orientations of SnO grains are random for the film deposited at 350°C, while the epitaxial film deposited at 600°C has an

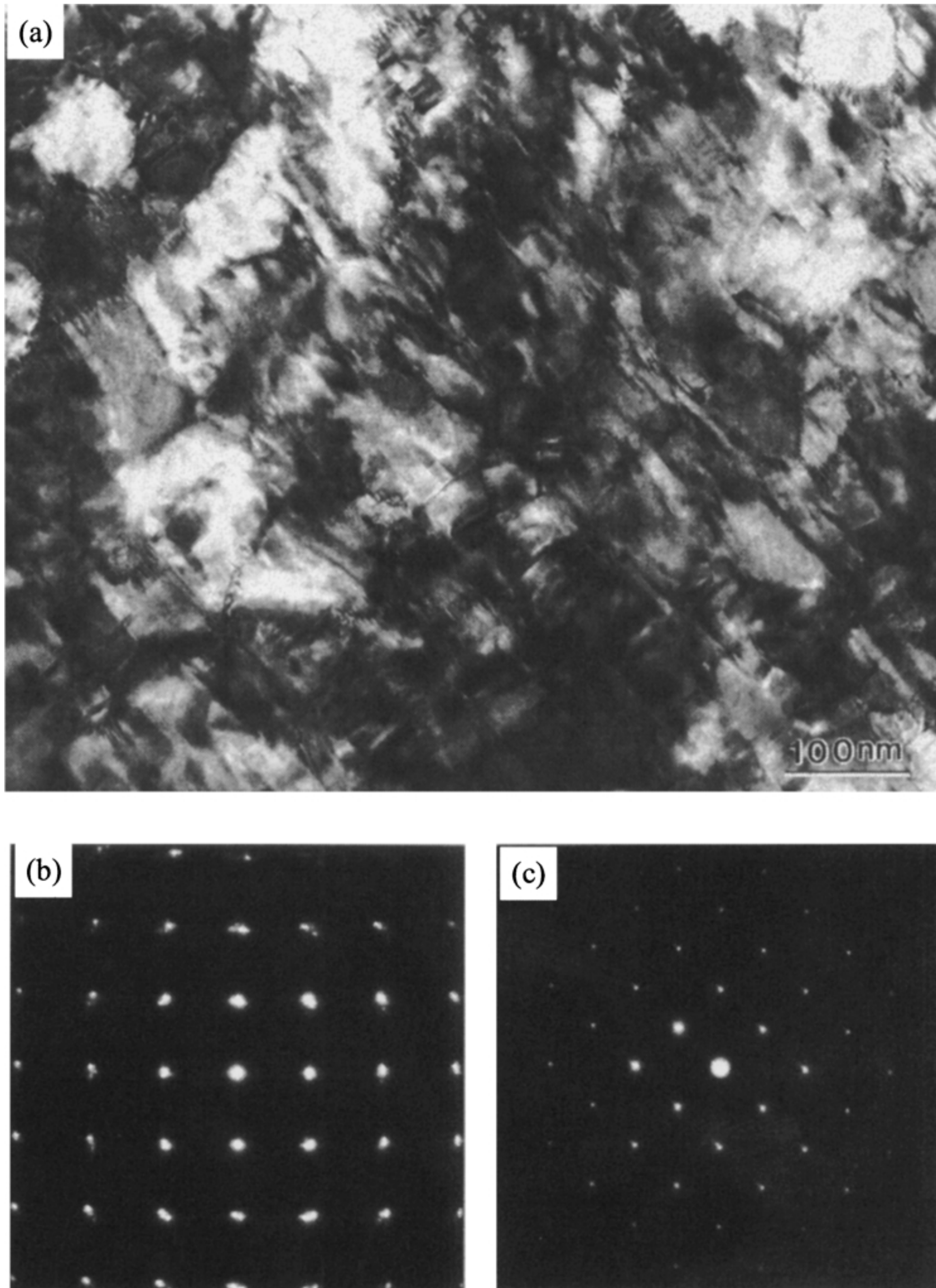

Fig. 5. (a) Bright field TEM image taken from a plan-view specimen of film E-600, showing that the thin film consists of grains with an average size of ∼150 nm. (b) Electron diffraction pattern taken from the area in (a), which is corresponding to the SnO [001] zone diffraction. (c) The corresponding electron diffraction pattern from the substrate.

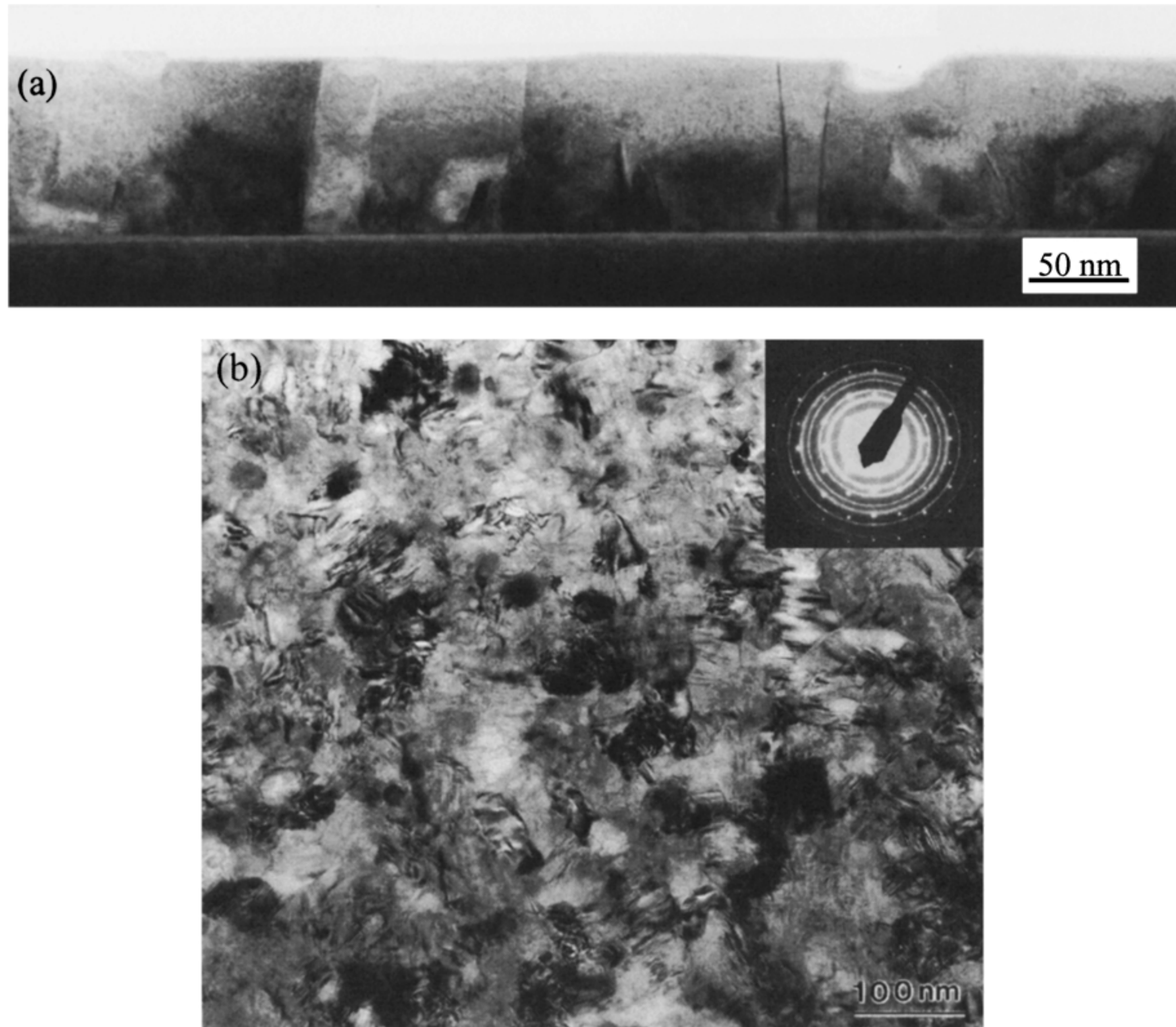

Fig. 6. (a) Bright field TEM image taken from a cross-section specimen of film E-350, showing a smooth surface. The film consists of polycrystalline grains with random shapes. (b) Plan-view TEM image taken from the same thin film as for (a). (c) Electron diffraction pattern taken from the plan-view specimen, including both reflections from the SnO film (rings) and reflections from the sapphire substrate (distinct spots).

in-plane orientation relationship with respect to the substrate of $(001)[100]_{SnO}//(\bar{1}012)[2\bar{2}01]_{Al_2O_3}$.

The formation of the α-SnO structure, instead of the rutile SnO_2 structure in e-beam deposition, is due to the fact that SnO_2 decomposes at high temperature in high vacuum with very low oxygen pressure during deposition [15]. The direct formation of the rutile SnO_2 phase requires a relatively high oxygen pressure which, however, is not suitable for the use of electron beam evaporation since the filament of the electron gun would be easily oxidized.

In the present work, the deposition temperature is a key factor in determining the microstructure and morphology of SnO films since all films were otherwise grown under the same conditions. Because most oxides do not fully wet the substrate in equilibrium at deposition temperature, film formation proceeds through the nucleation of islands or clusters on the substrate surface. These islands will then grow to cover the substrate surface and eventually coalesce to form a continuous film [23]. The mechanism involved in the formation of amorphous or crystalline states by condensation from

Table 1. Microstructure, composition and electrical resistivity of tin oxide films.

Film	Microstructure	[Sn]/[O] ratio	Resistivity (Ω cm)
E-RT	Amorphous	52.6/47.4	1.4×10^8
E-350	Polycrystalline α-SnO, randomly shaped grains with average grain size ≈30 nm. Out of plane texture: $(001)_{SnO}$// $(\bar{1}012)_{Al_2O_3}$	48.8/51.2	18
E-600	Epitaxial α-SnO, columnar grains with mean size of 150 nm. Orientation relationships: SnO(001)[100]// $Al_2O_3(\bar{1}012)$ $[2\bar{2}01]$	49.2/50.8	195

vapor phases primarily depends on the amount of time atoms or clusters of atoms interact to form bonds in metastable and/or stable structures [24]. At low temperatures, the vapor phase is rapidly quenched by deposition onto the cold substrate surface at a rate that limits bond formation. The limitation of establishing long-range order is further enhanced by the low surface diffusion due to the low temperature, which makes impinging atoms get trapped into clusters. As a result, a smooth surface consisting of small spherical agglomerates is formed in the amorphous film, as seen in Fig. 3(a).

When the deposition temperature is increased to above 350°C, the improved surface diffusion allows atoms to move and achieve long-range ordering during deposition, resulting in a crystalline structure. The film formed at such intermediate temperature (350°C in the present case) is polycrystalline even though there is a good lattice match between the film and the substrate. The film microstructure is also influenced by grain boundary mobility, which depends on temperature and atomic diffusion. Since most oxides have low diffusivities, films deposited at relatively low temperatures (350°C) have a large range of grain size distribution due to the low grain boundary mobility during cluster coalescence and film growth. However, this temperature (350°C) is high enough to create surface motion of the atoms, which results in a small surface roughness. The existence of texture in this film is probably due to the layered atomic structure along the [001] direction, which leads to a low (001) surface energy of SnO and a low film/substrate interfacial energy.

For films deposited at 600°C, the situation is different. Due to the improved surface mobility of atoms during deposition, epitaxial growth will be possible if there is a good lattice match between the film and the substrate. In the present system, the α-SnO phase is tetragonal with the PbO type structure ($a = 3.799$ Å, $c = 4.841$ Å, space group $P4/nmm$) [22], and the sapphire (α-Al_2O_3) has the rhombohedral structure ($a = 4.758$ Å, $c = 12.991$ Å, space group $P6$). Although these two materials belong to different

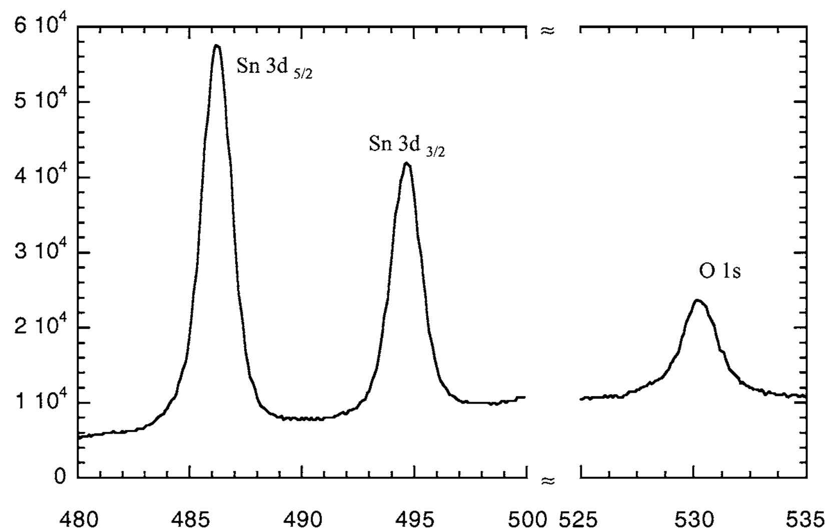

Fig. 7. XPS spectra taken from the film E-600, showing the binding energy peak position for Sn 3d and O 1s.

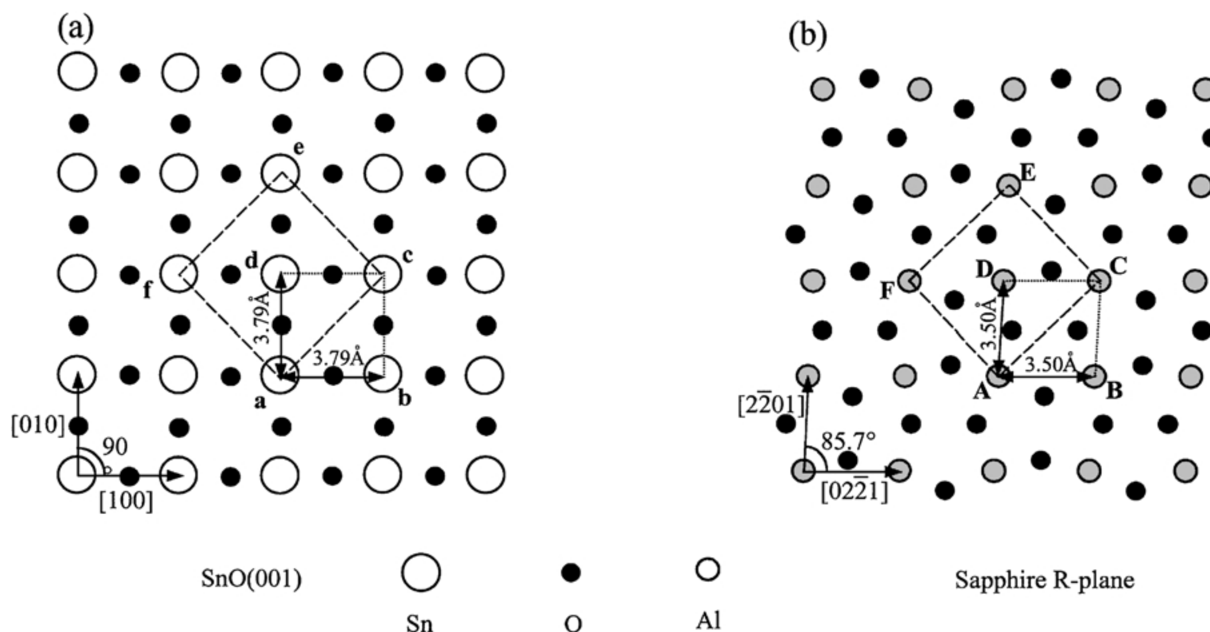

Fig. 8. Schematics showing the atomic configurations of the SnO (001) surface (a) and the sapphire ($\bar{1}$012) surface (b).

crystal systems, there are marked similarities between the SnO (001) surface and the sapphire ($\bar{1}$012) surface. As shown in Fig. 8, the interatomic distance $\overline{ab}$ (or $\overline{ad}$) is 3.79 Å in bulk SnO, whereas the corresponding distance $\overline{AB}$ (or $\overline{AD}$) is 3.50 Å in sapphire. If the SnO film grows on the sapphire with an orientation relationship of $[100]_{SnO}//[02\bar{2}1]_{Al_2O_3}$, i.e. $\overrightarrow{ab}//\overrightarrow{AB}$, the lattice mismatch along this direction, $\frac{\overline{ab}-\overline{AB}}{\overline{ab}}$, is 7.6%. Similarly, the SnO film may grow with $[100]_{SnO}//[2\bar{2}01]_{Al_2O_3}$, i.e. $\overrightarrow{ad}//\overrightarrow{AD}$. There is a rotating angle of $\sim$3.3° along the [001] direction between the SnO grains with these two different orientations because the $[02\bar{2}1]$ ($\overrightarrow{AB}$) and $[2\bar{2}01]$ ($\overrightarrow{AD}$) directions have an angle ($\angle$BAD) of 85.7°. A third possible orientation for the SnO film is: $[110]_{SnO}$ ($\overrightarrow{ac}$)//$[\bar{1}2\bar{1}0]_{Al_2O_3}$ ($\overrightarrow{AC}$) and $[\bar{1}10]_{SnO}$ ($\overrightarrow{af}$)//$[10\bar{1}1]_{Al_2O_3}$ ($\overrightarrow{AF}$). The lattice mismatch is 4.5% along the SnO $[1\bar{1}0]$ direction and 11% along the SnO [110] direction. Thus, the SnO film may consist of a number of grains which have orientations with respect to the substrate close to any of the above mentioned orientations. As a result, the electron diffraction taken along the [001] zone axis of such film will show a pattern such as that of Fig. 5(b). Grain boundaries existing in the film are mainly small angle boundaries.

The texture evolution and grain size evolution during film growth are dependent on grain boundary mobility, which is high at 600°C. The driving force for grain boundary motion is the minimization of grain boundary energy, film-substrate interfacial energy, film surface free energy, and misfit strain energy in the film. The increase of grain size will reduce the number of grain boundaries and thus decrease total grain boundary energy. Interface and grain boundary energies can also be reduced during growth through grain boundary migration, so that grains with high-energy orientations with respect to the substrate are consumed by the growth of grains with a low energy orientation. However, grain growth will cause the increase of grain size and thus increase the strain energy (if not relaxed) in the epitaxial film due to the existence of lattice mismatch. The balance of all aforementioned factors results in a restricted texture with a well-defined average grain size.

The difference in electrical conductivity can be discussed based on the microstructure and chemical composition of these films. E-350 has smaller grain size than E-600, which means E-350 has higher grain boundary density in the film. It is known that grain boundaries scatter electrical conducting carriers and thus reduce their mobility, resulting in the decrease of conductivity in the materials. Assuming that the microstructure is the main factor in determining the conductivity of the films, according to this mechanism,

the resistivity of film E-350 should be higher than that of film E-600. Obviously this is not the case from our measurements. Therefore, other more dominant mechanisms are likely to be responsible for the change in electrical transport behavior of these films.

The difference of [Sn]/[O] ratio in the films may explain this difference in resistivity. According to the Hall measurements of films studied, the crystalline SnO film is a p-type semiconductor, consistent with previous studies [25]. The conducting mechanism in the material is due to the excess of oxygen. Tin is normally in the form of Sn^{2+} in this material. If there is excess oxygen in the film, some cations will be transformed into Sn^{3+} in order to maintain electrical neutrality. This process can be considered as Sn^{2+} capturing a hole and forming weakbonded holes. These holes are located inside the bandgap near the top of the valence band and serve as acceptor states in the energy band structure. As a result, a p-type semiconductor is formed. According to the chemical composition determined by XPS, E-350 has more excess oxygen in the film ([Sn]/[O] = 48.8/51.2) than E-600 ([Sn]/[O] = 49.2/50.8), which means that the carrier (hole) density is lower in E-600, thus film E-600 shows much higher resistivity (195 Ω cm) than E-350 (18 Ω cm).

5. Conclusions

Tin oxide thin films were deposited on the ($\bar{1}012$) sapphire (R-cut) substrates by electron-beam evaporation of pure ceramic SnO_2 source. Thin films with different microstructures were fabricated by varying deposition temperatures while other processing conditions remained unchanged. Films deposited at low temperatures are amorphous while those grown at temperatures above 350°C have a crystalline α-SnO phase which has the PbO-type structure. Epitaxial SnO thin films were obtained when deposited at 600°C, with the orientation relationship with respect to the substrate of SnO [100](001)//sapphire [$2\bar{2}01$] ($\bar{1}012$). Both cross-section TEM and AFM examinations showed that the thin film surface morphology depended on the deposition temperature. XPS analyses showed that the chemical compositions in tin oxide films are influenced by deposition temperature. Resistivity measurements revealed that amorphous SnO film is insulating, while crystalline SnO films are conductive. However, the resistivity of epitaxial SnO film (E-600) was one magnitude higher than polycrystalline SnO film (E-350). The difference in electrical properties were ascribed to the change in the [Sn]/[O] ratio in the films.

Acknowledgments

The authors gratefully acknowledge the financial support of the National Science Foundation DMR 9875405 (CAREER—XQP), the College of Engineering at the University of Michigan-Ann Arbor, and the Applied Materials Company.

References

1. W. Göpel, J. Hesse, and J.N. Zemel (eds.), *Sensors—A Comprehensive Survey*, Vol. 2. Chemical and Biochemical Sensors (Parts 1 and 2) (VCH Weinheim, New York, 1991).
2. K. Ihokura and J. Watson, *The Stannic Oxide Gas Sensor—Principles and Applications* (CRC Press, Boca Raton, FL, 1994).
3. G. Advani and A. Jordan, *J. Electrochem. Soc.*, **123**, 29 (1990).
4. N. Yamazoe, New approaches for improving semiconductor gas sensors, in *Proc. 3rd Int. Meet. Chem. Sensors*, Cleveland, OH, USA, Sept. 24–26, 1990, pp. 3–8.
5. C. Xu, J. Tamaki, M. Miur, and N. Yamazoe, *Sensors and Actuators B*, **3**, 147 (1991).
6. N.Y. Shishkin, I.M. Zharsky, V.G. Lugin, and V.G. Zarapin, *Sensors and Actuators B*, **48**, 403 (1998).
7. M.C. Horrillo, P. Serrini, J. Santos, and L. Manes, *Sensors and Actuators B*, **45**, 193 (1997).
8. S. Semancik and R.E. Cavicchi, *Thin Solid Films*, **206**, 81 (1991).
9. M.H. Reddy and A.N. Chandorkar, *Sensors and Actuators B*, **9**, 1 (1992).
10. W.I. Cho, H. Jang, and S.R. Lee, *Scripta Metallurgica et Materialia*, **32**, 815 (1995).
11. R. Larciprete, E. Borsella, P. De Padova, P. Perfetti, and C. Crotti, *Journal of Vacuum Science and Technology A*, **15**, 2492 (1997).
12. D. Liu, Q. Wang, H.L.M. Chang, and H. Chen, *Journal of Material Research*, **10**, 1516 (1995).
13. F.M. Amanullah, K.J. Pratap, and V. Hari Babu, *Materials Science and Engineering B*, **52**, 93 (1998).
14. K. Murakami, I. Yagi, and S. Kaneko, *Journal of American Ceramic Society*, **79**, 2557 (1996).
15. L. Holland, *Vacuum Deposition of Thin Films* (Chapman & Hall, London, 1963), pp. 446–450.
16. W. Göpel and K.D. Schierbaum, *Sensors and Actuators B*, **26**, 1 (1995).
17. J.-G. Zheng, X.Q. Pan, M. Schweizer, U. Weimar, W. Göpel, and M. Rühle, *Phil. Mag. Lett.*, **73**, 93 (1996).
18. J.-G. Zheng, X.Q. Pan, M. Schweizer, F. Zhou, U. Weimar, W. Göpel and M. Rühle, *J. Appl. Phys.*, **79**, 7688 (1996).
19. J.-G. Zheng, X.Q. Pan, M. Schweizer, U. Weimar, W. Göpel and M. Rühle, *J. Mater. Sci.*, **31**, 2317 (1996).
20. X.Q. Pan and J.G. Zheng, "Microstructure of and crystal defects in nanocrystalline tin dioxide thin films, in *Polycrystalline Thin Films—Structure, Texture, Properties and Applications III*, edited by S.M. Yalisove, B.L. Adams, J.S. Im, Y. Zhu, and F.R.

Chen (Mater. Res. Soc. Proc. Vol. 472, Pittsburgh, PA, 1997), pp. 87–92.
21. S.K. Song, J.S. Cho, W.K. Choi, H.J. Jung, D. Choi, J.Y. Lee, H.K. Baik, and S.K. Koh, *Sensors and Actuators B*, **46**, 42 (1998).
22. J. Pannetier and G. Denes, *Acta Crystallogr. B*, **36**, 2763 (1980).
23. C. Thompson and R. Carel, *Materials Science and Engineering B*, **32**, 211 (1995).
24. L.L. Kazmerski, *Polycrystalline and Amorphous Thin Films and Devices* (Academic Press, New York, 1980).
25. Z.D. Guan, Z.T. Zhang, and J.S. Jiao, *Physical Properties of Non-organic Materials* (Tsinghua University Press, Beijing, China, 1992).